Journal of 先进陶瓷 Advanced Ceramics
ISSN 2226-4108
CN 10-1154/TQ
清华大学出版社 Tsinghua University Press
SciOpen

J Adv Ceram 2026, **15**: 9221366

https://doi.org/10.26599/JAC.2026.9221366

Research Article

Phase-transition-regulated precipitation–densification to achieve a hardness–toughness synergy in in-situ composite ceramics of triphase silicon nitride

Shucheng Liu[1], Bingtao Feng[1], Zhaodong Liu[1], Bingbing Liu[1], Hu Tang[1],*

State Key Laboratory of High Pressure and Superhard Materials, Synergetic Extreme Condition High-Pressure Science Center, College of Physics, Jilin University, Changchun, China

* Corresponding author.

E-mail: hutang@jlu.edu.cn

Received: June 28, 2026; Revised: August 22, 2026; Accepted: August 28, 2026

Abstract: Structural materials generally struggle to simultaneously achieve high hardness and toughness. Composites, as a “complementary advantages” strategy, aim to optimize the synergy between hardness and toughness through the regulation of microstructure and composition. However, conventional composite strategies commonly suffer from insufficient interfacial compatibility and

inhomogeneous distribution of reinforcing phases, limiting the full realization of multiphase synergistic strengthening effects. Here we successfully synthesized homogeneous triphase silicon nitride ceramics via an in-situ composite strategy under high-temperature and high-pressure (HPHT) conditions, achieving synergistic enhancement in hardness and toughness with a Vickers hardness of 26.34 ± 0.61 GPa and a fracture toughness of 6.02 ± 0.48 MPa·m$^{1/2}$. The superior mechanical properties are attributed to the precise regulation of microstructural evolution through the phase-transition pathway, establishing a sequential precipitation–densification mechanism that regulates γ phase precipitation and transformation kinetics while allowing concurrent α-to-β transformation and progressive densification. Specifically, nanoscale γ phase particles significantly enhance the hardness, whereas high-aspect-ratio β grains effectively improve fracture toughness through crack bridging and crack arrest and reinitiation mechanisms. This phase-transition-regulated in-situ composite strategy based on silicon nitride polymorphs provides new insights into the microstructural engineering for synergistic hardening and toughening of advanced structural ceramics.

Keywords: silicon nitride, microstructural engineering, phase transition, composite, HPHT

1. Introduction

Ceramics generally exhibit high hardness owing to their strong covalent and ionic bonds, which also endow them with excellent resistance to temperature, corrosion, and wear [1–5]. Consequently, they have been widely applied in storage devices, biomedical implants, and extreme-environment applications [6–9]. Unfortunately, the strong and oriented bonds also lead to intrinsic brittleness, severely limiting their safety-critical applications [10–12]. Therefore, the design of structural materials simultaneously possessing high hardness and toughness remains an urgent challenge. Researches on ceramic toughening began in the 1970s with zirconia ceramics and ceramic matrix composites (CMCs) [13,14]. Fundamentally, these strategies rely on microstructural engineering to achieve precise regulation of crystal structures, chemical compositions, and interfaces, thereby introducing crack

branching, crack bridging, crack deflection, and pull-out mechanisms to dissipate fracture energy and effectively alleviate stress concentration at crack tips [15–19].

Silicon nitride, a representative brittle ceramic with strong covalent bonding, exists in α, β, and γ polymorphs [20–22]. Among them, α phase consists of equiaxed grains and exhibits a hardness of ~20 GPa [23,24]. In contrast, β phase possesses rod-like grains with high aspect ratios and has been extensively utilized for ceramic toughening in industrial applications, but is limited to a relatively low hardness of ~16 GPa [25–27]. In addition, β-Si_3N_4 has also been exploited to fabricate hollow and porous ceramic structures with high mechanical strength and attractive functional properties [28,29]. Owing to the structural similarity and high lattice compatibility between α and β phases, extensive studies have focused on α/β biphasic silicon nitride ceramics combining hardness and toughness [30,31]. Although substantial improvements in fracture toughness have been achieved, hardness remains limited to ~20 GPa. In comparison, the high-pressure γ phase with a spinel structure exhibits an exceptional hardness exceeding 35 GPa [32], rendering it a promising candidate for enhancing the hardness of silicon nitride ceramics. Although γ-Si_3N_4 exhibits a relatively low fracture toughness of ~3.5 $MPa \cdot m^{1/2}$, its combination with Hf_3N_4 has enabled nanocomposites with simultaneously enhanced hardness and fracture toughness [33]. However, studies on triphase silicon nitride ceramics remain largely unexplored because the rapid phase-transition kinetics hinder the capture of intermediate states, while the significant volume shrinkage accompanying the transformation imposes substantial challenges on densification and interfacial bonding.

Here we establish a sequential precipitation–densification mechanism that exploits the distinct phase-transition kinetics of silicon nitride polymorphs to regulate phase evolution and microstructural development. Using this strategy, we successfully fabricated homogeneous triphase silicon nitride ceramics under high pressure, in which γ phase precipitation precedes substantial densification while the α-to-β transformation proceeds concurrently. The obtained ceramics exhibit a Vickers hardness of 26.34 ± 0.61 GPa, significantly exceeding that of α phase silicon nitride, together with a markedly

improved fracture toughness of 6.02 ± 0.48 MPa·m$^{1/2}$. The superior hardness originates from nanoscale γ phase particles and strong coherent interfacial bonding, whereas the toughening behavior arises from crack bridging by high-aspect-ratio β grains and stress redistribution at crack tips. This phase-transition-regulated strategy provides a general route to integrate hard and tough constituents for the simultaneous optimization of hardness and fracture toughness in polymorphic structural ceramics.

2. Experimental methods

2.1 Sample processing and preparation

2.1.1 Pre-compression and pretreatment of samples

Silicon nitride powder (purity >99.9%, Aladdin) was used as the starting material. The powder consisted of 93.3 wt.% α phase and 6.7 wt.% β phase, with the impurity contents reported in our previous work [31]. The powder was cold-pressed into pellets using a 4 mm diameter mold under a pressure exceeding 300 MPa. The compacted samples were first heated at 600 °C for 1 h in a tube furnace under flowing Ar atmosphere to remove adsorbed moisture and impurities. Subsequently, the pretreated samples were subjected to HPHT treatments in a 6 × 14 MN (six anvils, 14 MN maximum load per anvil) large-volume cubic press at 5 GPa. The α-pillar was synthesized at 1500 °C with a dwelling time of 10 min, whereas the β-pillar was obtained at 2000 °C for 30 min. The heating rate was maintained at 100 °C s^{-1}, and the compression/decompression rate was 0.07 MPa s^{-1}. The recovered α- and β-pillars were mechanically polished using diamond abrasive papers. Cylindrical samples with dimensions of 1.9 mm in diameter and 1.8 mm in height were extracted from the central region of the pillars by laser cutting. The samples were then ultrasonically cleaned in acetone to remove surface contaminants introduced during laser machining. The cleaned samples were used as dense precursors for the subsequent high-pressure synthesis experiments.

2.1.2 High-pressure synthesis experiments

High-pressure synthesis experiments were conducted at 15 GPa and 1100–1900 °C using a Kawai-type multianvil press with a 10/5 assembly at the B1 and B3 stations of the Synergetic Extreme

Condition User Facility (SECUF), Jilin University [34]. Tungsten carbide anvils and MgO + 5 wt.% Cr_2O_3 octahedra were employed as the pressure-transmitting medium. Pressure was determined using a pre-calibrated pressure curve, and temperature was monitored using a W97Re3–W75Re25 (type-D) thermocouple. The target pressure was reached over 8 h, followed by heating at a rate of 100 °C min^{-1}. After the high-temperature dwelling stage, the samples were cooled to 500 °C at a rate of 100 °C min^{-1} and maintained at 500 °C during decompression. Heating was maintained until 3 h before the completion of pressure release, after which the samples were allowed to cool naturally. The recovered samples were obtained after a total decompression process lasting more than 10 h.

2.2 Structural characterization

X-ray diffraction (XRD) patterns were collected using an R-AXIS RAPID X-ray diffractometer (Rigaku, Cu Kα radiation) operated at 30 kV and 40 mA, and a SmartLab SE diffractometer (Rigaku, Cu Kα radiation) equipped with a D/teX Ultra250 (0D/1D) detector. The α, β, and γ phases were identified using PDF 01-083-0700, 01-073-3032, and 01-075-8455, respectively. The Rietveld refinement method was employed to quantify the phase contents by using the generalized structure analysis system (GSAS) [35]. Raman spectra were acquired using a LabRAM HR Evolution spectrometer with 532 and 785 nm laser excitation sources over the spectral range of 150–1150 cm^{-1}. The fracture surfaces and crack morphologies were characterized by scanning electron microscopy (SEM, Regulus-8100, Hitachi Ltd.) operated at an accelerating voltage of 5 kV. Nanoscale structural characterization was performed by focused ion beam (FIB) milling using a Thermo Scientific Helios 5 CX system. Lamellae were extracted perpendicular to the stress-free region. Phase distribution and orientation relationships were further analyzed by 4D scanning transmission electron microscopy (4D-STEM) orientation characterization (Thermo Scientific Spectra 200 equipped with an Electron Microscope Pixel Array Detector, EMPAD) using a precession angle of 1°, a step size of 3 nm, and an exposure time of 20 ms, together with transmission electron microscopy (TEM, FEI Tecnai F20).

2.3 Computational methods

To evaluate thermodynamic stability, we performed thermodynamic integration (TI) for the α-β phase boundary. Configurational sampling was assisted by MatterSim [36], and iterative training produced a standard neuroevolution potential (NEP) [37,38] trained on DFT data. TI was conducted with this standard NEP using GPUMD [39,40]. For kinetic barriers, we employed the solid-state nudged elastic band (SSNEB) method [41] for the α-to-γ and β-to-γ transformations, using an SSNEB-NEP trained on pathway configurations generated by SSNEB with TSASE built upon the Atomic Simulation Environment (ASE) [42]. DFT reference data were obtained with the PAW method [43,44], PBE functional [45], and Grimme D3 corrections [46,47] in VASP [48,49], using a 900 eV cutoff and 10^{-6} eV convergence. Detailed procedures are given in the ESM.

2.4 Mechanical characterization

Vickers hardness measurements were performed at loads of 1.96, 4.9, 9.8, and 19.6 N with a dwell time of 10 s. At least five valid indentations were analyzed at each load to calculate the average hardness values and standard deviations. Fracture toughness was evaluated from at least five valid indentations at 19.6 N, and the average fracture toughness and standard deviation were calculated accordingly. Nanoindentation tests were conducted using a KLA Nano Indenter G200 with a maximum load of 500 mN.

Vickers hardness, H_V (GPa), was calculated using:

$$H_V = 1854.4F/L^2 \quad (1)$$

where F is the applied load (N), L is the average length of the diagonal of indentation (μm).

The fracture toughness obtained from indentation tests, K_{IC} (MPa·m$^{1/2}$), was calculated using [50]:

$$K_{IC} = 0.016(E/H_V)^{0.5} F/c^{1.5} \quad (2)$$

where E is the Young's modulus (GPa), H_V is the Vickers hardness (GPa), F is the applied load (N), c is the average length of the radial cracks (μm).

3. Results and discussion

3.1 Phase-transition pathways and high-pressure phase diagram

To investigate the phase-transition pathways of α- and β-Si_3N_4 under HPHT conditions, dense single-phase silicon nitride pillars were first synthesized at a relatively low pressure of 5 GPa. XRD patterns (Fig. 1(a)) and SEM images (Fig. 1(c)), together with the grain-size distribution shown in Fig. 1(f), confirm that the starting material consists predominantly of α-Si_3N_4 with a minor amount of β phase. Based on our previous work [31], the α- and β-pillars were synthesized at 1500 and 2000 °C, respectively, and the assembly configuration is illustrated in Fig. 1(b). Polished-and-etched SEM characterization of the synthesized samples (Figs. 1(d)-1(e)), together with the corresponding grain-size distributions (Figs. 1(g)-1(h)), reveals distinct microstructural evolution in the two pillars. For the α-pillar, in the absence of significant phase transformation, grain fragmentation under high pressure results in substantial grain refinement, with the average grain size decreasing markedly from 0.71 to 0.26 μm. In contrast, the β-pillar undergoes pronounced densification, accompanied by grain growth at elevated temperature, with the average grain size increasing to 1.21 μm. These pillars were subsequently employed to explore the phase-transition pathways toward the γ phase under 15 GPa and 1100–1900 °C. The detailed assembly configuration and pressure calibration curve are shown in Fig. S2 in the ESM.

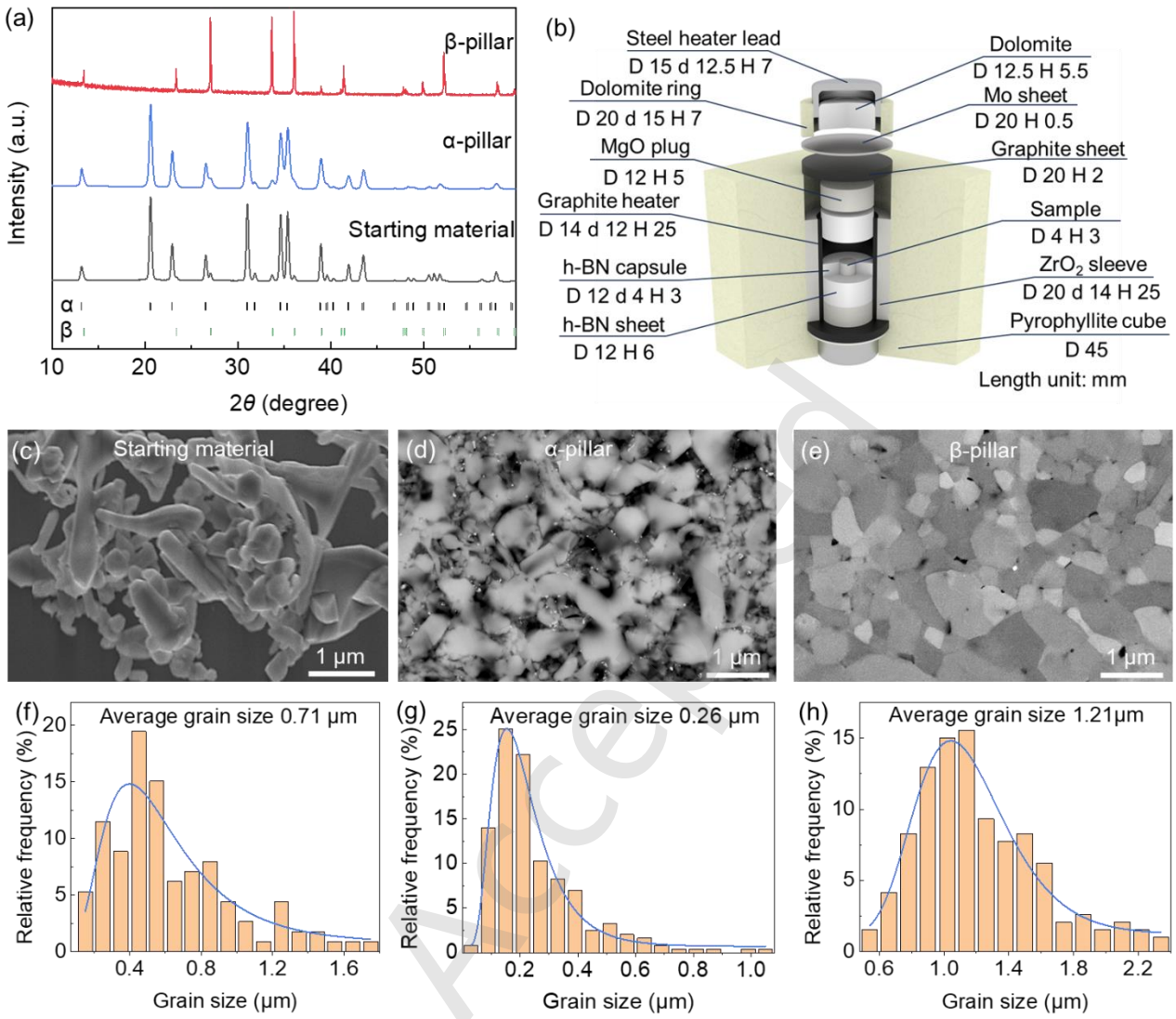

Fig. 1. Pretreatment of the starting material and microstructural characterization. (a) XRD patterns of the starting material and the sample pre-compacted under HPHT conditions. (b) Schematic illustration of the assembly configuration in a 6 × 14 MN large-volume cubic press. (c–e) SEM images of the starting material and polished-and-etched surfaces of the α- and β-pillars, respectively, acquired in the backscattered electron (BSE) mode. (f–h) Corresponding grain-size distributions for the microstructures shown in (c–e), respectively.

Fig. 2a and Fig. S3 in the ESM present the XRD patterns of samples synthesized using α-pillars as precursors at different temperatures. Rietveld refinement of the XRD patterns of the triphasic samples provides quantitative phase fractions, as summarized in Fig. S4 in the ESM and Table 1. Unexpectedly, a small amount of γ phase (6.8 wt.%) forms at only 1100 °C. With increasing temperature to 1300 °C,

the γ phase content increases only slightly to 8.7 wt.%. The gradual increase in γ phase fraction at 1100–1300 °C suggests that γ phase nucleation can occur at relatively low temperatures, whereas substantial phase transformation requires higher temperatures. At 1500 °C, the α phase undergoes simultaneous α-to-β and α-to-γ transformations, resulting in 17.0 wt.% β phase and 14.1 wt.% γ phase. Upon further heating to 1600 °C, the α-to-β transformation becomes dominant, with the β phase content increasing from 17.0 to 37.3 wt.%, indicating strong competition between the transformation pathways and their pronounced temperature dependence. At 1700 °C, only the γ phase is detected, indicating the formation of bulk single-phase γ-Si_3N_4. Raman spectra (Figs. 2(b)-2(c)) further confirm the phase evolution observed by XRD. Notably, with increasing temperature, the Raman bands of the α phase within the 490–520 cm^{-1} range gradually broaden and shift toward higher wavenumbers, indicating variations in the low-intensity shoulder band at 512 cm^{-1} [51]. Simultaneously, the Raman-active T_{2g} mode of γ phase at 522 cm^{-1}, dominated by the vibration of nitrogen ions, progressively intensifies, confirming the formation of γ phase [52,53].

In contrast, the β-pillars exhibited a distinctly different phase-transition behavior. The XRD patterns (Fig. 2d) and Raman spectra (Fig. 2e) of samples synthesized from β-pillars at different temperatures indicate that the β-to-γ phase transition initiates at 1825 °C. No γ phase was detected at 1800 °C, whereas Rietveld refinement at 1825 °C revealed 91.7 wt.% β phase and 8.3 wt.% γ phase (Fig. S5 in the ESM and Table 1). This abrupt onset of γ phase formation suggests a relatively high nucleation barrier, followed by rapid β-to-γ transformation once nucleation is initiated. Moreover, Raman analysis of the sample synthesized at 1825 °C, which contained a small amount of residual β phase, shows that the E_{1g} mode at 522 cm^{-1} and the T_{2g} mode at 840 cm^{-1} shift toward lower wavenumbers (Fig. 2(f)). These modes are mainly associated with vibrations of nitrogen ions and tetrahedrally coordinated Si atoms, and their redshift implies the introduction of defects during the phase-transition process [52–54].

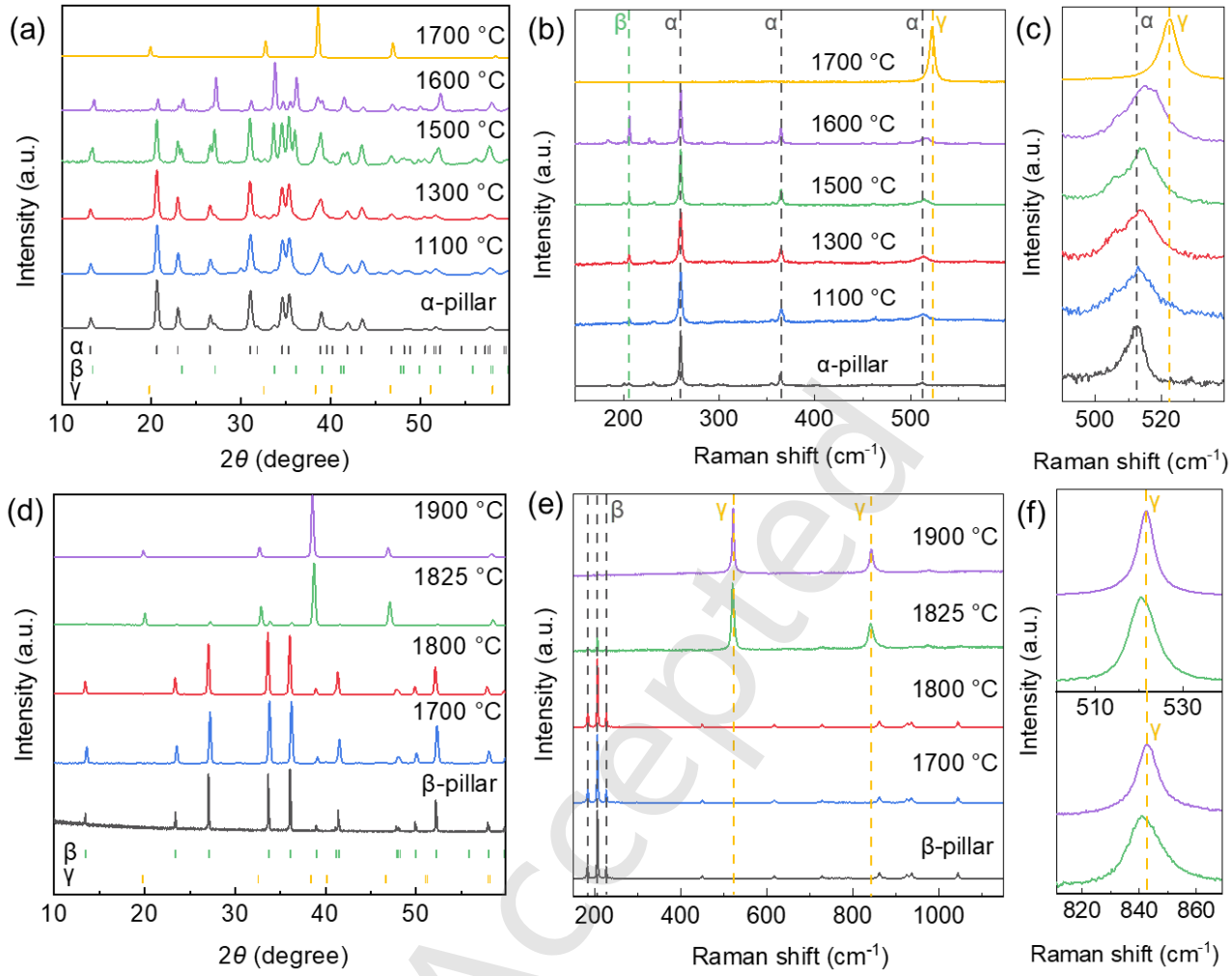

Fig. 2. Phase evolution of the α- and β-pillars at different sintering temperatures under 15 GPa. (a,d) XRD patterns of the samples derived from α- and β-pillars, respectively. (b,e) Raman spectra of the corresponding samples shown in (a) and (d), respectively. (c) Enlarged region of (b) in the 490–520 cm^{-1} range. (f) Enlarged regions of (e) in the 500-540 cm^{-1} (top) and 810-870 cm^{-1} (bottom) ranges for the samples synthesized at 1825 and 1900 °C.

Table 1. Rietveld-refined phase fractions of all biphasic and triphasic samples shown in Fig. 2. The phase composition of the starting material was obtained from our previous work [31].

Precursor	Experiment condition	Phase composition	α content (wt.%)	β content (wt.%)	γ content (wt.%)
Starting material		α+β	93.3	6.7	
α-pillar	15 GPa 1100 ℃	α+β+γ	86.4	6.8	6.8
α-pillar	15 GPa 1300 ℃	α+β+γ	83.6	7.7	8.7

α-pillar	15 GPa 1500 °C	α+β+γ	68.9	17.0	14.1
α-pillar	15 GPa 1600 °C	α+β+γ	42.9	37.3	19.8
β-pillar	15 GPa 1825 °C	β+γ		91.7	8.3

Based on the above experimental results and extensive previous studies [22,31,32,55–58], HPHT phase diagrams for the α and β phases were constructed in Fig. 3. At pressures below 8 GPa, the α-to-β transition occurs within the temperature range of 1500–1700 °C. To minimize the effects of sintering additives, grain size, and holding time, additional experiments were conducted at 5 GPa and 1500–1900 °C (Fig. S6 in the ESM), revealing the onset of the α-to-β transformation at 1700 °C. At 15 GPa, the α-to-β transition temperature decreases to ~1500 °C. Together with the calculated thermodynamic phase diagram (Fig. S7 in the ESM), these experimental results indicate that the α/β phase boundary shifts toward lower temperatures with increasing pressure, demonstrating that pressure promotes the α-to-β transformation. When the temperature exceeds 1700 °C at pressures above 12.9 GPa, the γ phase becomes the only thermodynamically stable phase. As shown in Fig. 3(b), the β-to-γ phase transition occurs at 1825 °C under 15 GPa, substantially higher than the α-to-γ transition temperature. To further understand this difference, we performed SSNEB calculations to quantify the pathway-dependent transformation barriers for the α-to-γ and β-to-γ phase transformations. The calculated barriers are approximately 647 and 956 meV $atom^{-1}$, respectively, at 15 GPa (Fig. S8 in the ESM). The substantially higher barrier for the β-to-γ pathway indicates that the β-to-γ transformation is kinetically more hindered under the investigated conditions, consistent with its higher transformation temperature compared with the α-to-γ pathway.

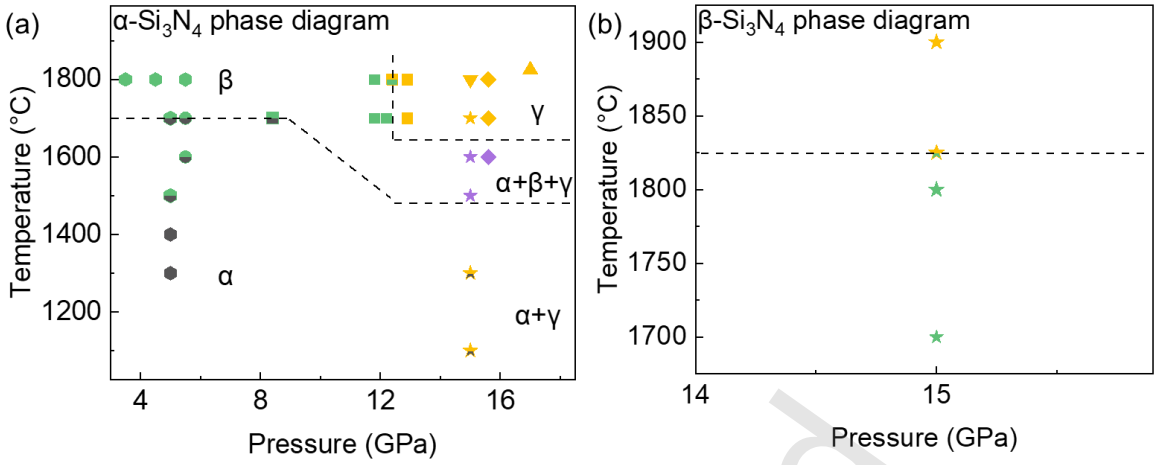

Fig. 3. Temperature–pressure phase diagram of silicon nitride. (a) α-Si_3N_4. (b) β-Si_3N_4. Gray, green, yellow, and purple symbols represent the α, β, γ, and triphase compositions, respectively. Different symbol shapes denote data from different references. All pentagrams in the diagrams represent the experimental conditions investigated in this work.

3.2 Sample synthesis and microstructural characterization

Limited by the rapid phase-transition kinetics of γ phase, a strategy involving nucleation above the transition barrier followed by low-temperature growth was adopted to fabricate in-situ composite ceramics of silicon nitride, containing a high fraction of γ phase using α- and β-pillars as precursors. The detailed experimental conditions were summarized in Table 2. SN-11 was synthesized from β-pillar owing to its relatively simple phase-transition pathway. The XRD pattern and Raman spectra (Fig. 4) indicate that SN-11 is a β/γ biphasic composite ceramic dominated by the β phase, with Rietveld refinement yielding phase fractions of 63.2 wt.% β phase and 36.8 wt.% γ phase (Fig. S9(a) in the ESM). After careful polishing, optical microscopy images (Fig. S10(a) in the ESM) reveal that γ phase is uniformly distributed within the β phase matrix in the form of precipitates with sizes of 3–5 μm. Subsequent Vickers hardness measurements on the polished surface show that the Vickers hardness of SN-11 (Fig. S10(b) in the ESM) slightly decreases compared with the original β-Si_3N_4, from 17.28 to 15.44 GPa (Table 2). Combined with the indentation morphology (Fig. S10(b) in the

ESM), this degradation is mainly attributed to the excessively large γ phase precipitates and the poor interfacial bonding between the β and γ phases caused by their large thermal-expansion mismatch [54].

Table 2. Experimental conditions, phase compositions, and mechanical properties of silicon nitride samples. The reported Vickers hardness and indentation fracture toughness values were obtained at an indentation load of 19.6 N.

Sample	Precursor	Experiment condition	Phase composition	H_V (GPa)	K_{IC} (MPa·m$^{1/2}$)
SN-11	β-pillar	15 GPa 1850 °C 1 min 1750 °C 10 min	β+γ	15.44±0.85	2.56±0.13
SN-14	α-pillar	15 GPa 1750 °C 1 min 1650 °C 10 min	α+β+γ	26.34±0.61	6.02±0.48
β-Si_3N_4	α-pillar	5 GPa 2000 °C 30 min	β	17.28±0.26	2.71±0.24
γ-Si_3N_4	α-pillar	15 GPa 1700 °C 60 min	γ	32.03±0.29	3.92±0.21

Subsequently, α-pillars were employed as precursors to fabricate the α/β/γ triphase in-situ composite ceramic (SN-14) by exploiting the temperature-dependent differences between the α-to-β and α-to-γ phase transformations under high pressure (experimental conditions are listed in Table 2). The two-step synthesis was designed to regulate the relative kinetics of γ phase nucleation and β phase formation. Specifically, the sample was first treated at 1750 °C for 1 min, above the experimentally determined γ phase transformation temperature, to promote rapid γ phase nucleation while limiting prolonged high-temperature exposure and excessive grain growth. The temperature was then lowered to 1650 °C and maintained for 10 min, below the temperature for rapid γ phase transformation, to slow γ phase growth and mitigate abrupt transformation-induced shrinkage, while allowing the α-to-β transformation to proceed. This sequential thermal treatment enables phase precipitation to precede subsequent densification while allowing the α-to-β transformation to proceed. As a result, SN-14 develops a refined triphase microstructure dominated by the β and γ phases (Fig. 4), with phase fractions of 21.3

wt.% α phase, 40.2 wt.% β phase, and 38.5 wt.% γ phase determined by Rietveld refinement (Fig. S9(b) in the ESM).

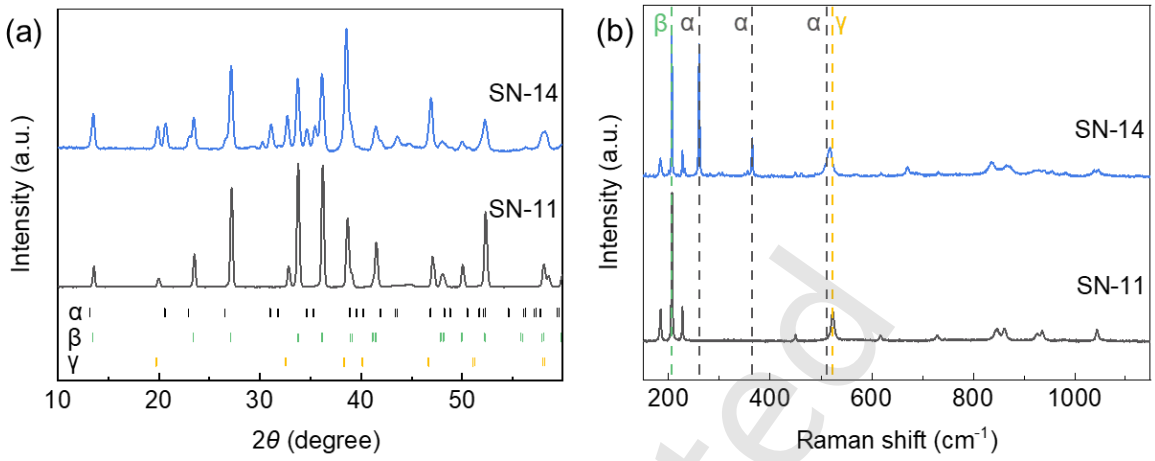

Fig. 4. Fabrication of multiphase silicon nitride composites using α- and β-pillars as precursors. (a,b) XRD patterns and Raman spectra of the synthesized samples, respectively.

To investigate the phase fractions and microstructure of SN-14, a FIB sample (Fig. S11(a) in the ESM) was prepared from a stress-free region. 4D-STEM orientation characterization was performed in the red- and blue-boxed regions of the FIB sample, yielding phase fractions of 18 wt.% α phase, 43 wt.% β phase, and 39 wt.% γ phase, and 22 wt.% α phase, 41 wt.% β phase, and 37 wt.% γ phase, respectively (Figs. 5(a)-5(b) and S11(b)-S11(c) in the ESM). The close agreement between the phase fractions obtained from the two regions and their good consistency with the Rietveld refinement results (Fig. S9(b) in the ESM) further confirm the homogeneous phase distribution throughout the SN-14 sample. Since both β and γ phases originate from the phase transformation of α phase, micron-sized α/γ and α/β biphasic grains were selected for TEM characterization. Figure 5(c) shows the morphology and phase distribution of an α/γ biphasic grain. Figs. 5(d)-5(f) and Figs. 5(g)-5(i) present the selected-area electron diffraction (SAED) patterns and atomic-resolution images along the [1-2-1] direction, respectively, revealing that the γ phase retains the same crystallographic orientation as the parent α phase during transformation. High-resolution transmission electron microscopy (HRTEM) images of the interfacial region (Figs. S11(d)-S11(e) in the ESM) further reveal a high density of interfacial defects and abundant stacking faults within the γ phase, arising from atomic migration during the phase

transition. Moreover, owing to the high similarity of diffraction patterns between α and γ phases along the [1-2-1] direction under coherent relationships (Fig. S11(f) in the ESM), the γ and α phases were further tilted to the $[111]_{\gamma}$ and $[001]_{\alpha}$ zone axis, respectively, to confirm their phase identities (Figs. S11(g)-S11(h) in the ESM). Figures 5(j)-5(k) show the morphology and phase distribution of an α/β biphasic grain. Combined with the orientation relationships shown in Figs. 5(l)-5(o), the results suggest that the α-to-β phase transition under 15 GPa remains consistent with the coherent transformation mechanism reported under low-pressure conditions [31]. Together, these observations demonstrate that slowing the γ phase transformation mitigates abrupt transformation shrinkage, while the concurrent α-to-β transformation contributes to overall densification. Despite the presence of interfacial defects arising from atomic rearrangement during the phase transformation, the interfaces retain well-defined crystallographic relationships. Collectively, these results establish a sequential precipitation–densification mechanism for regulating phase evolution and interfacial structure.

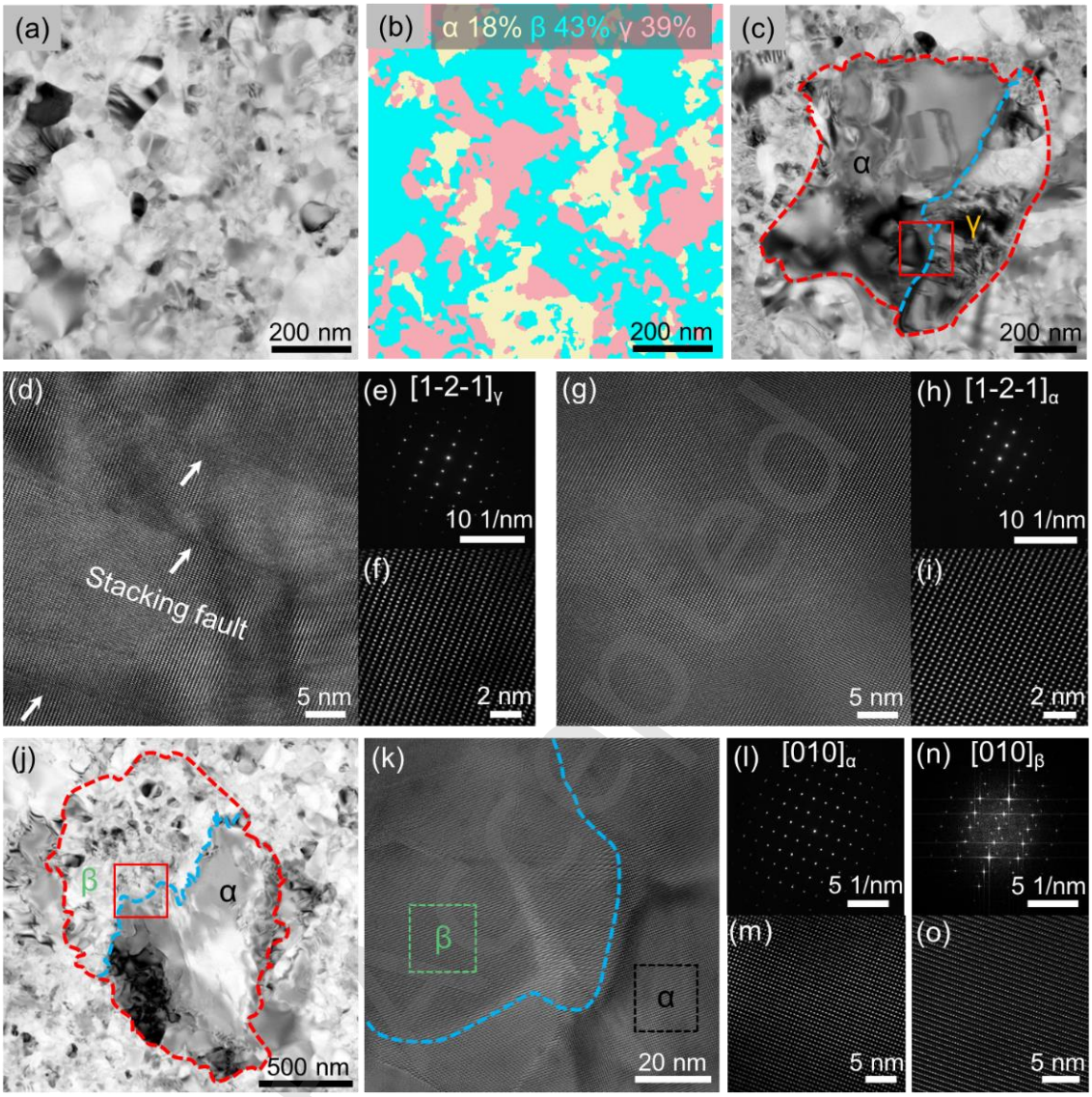

Fig. 5. Compositional analysis and microstructural characterization of SN-14. (a) Bright-field image of the region outlined by the red box in the FIB sample (Fig. S11(a) in the ESM). (b) 4D-STEM orientation analysis results of the region shown in (a), and the values represent weight fractions. (c) Bright-field image of the α/γ biphasic grain. The red dashed line outlines the overall grain morphology, the blue dashed line indicates the phase boundary, and the red boxed region corresponds to the characterization areas shown in (d–i). (d–f) and (g–i) HRTEM images, SAED patterns, and atomic-resolution images of the γ and α phases along the [1-2-1] zone axis, respectively. (j) Bright-field image of the α/β biphasic grain. The red dashed line outlines the overall grain morphology, and the blue dashed line indicates the phase boundary. (k) HRTEM image of the region outlined by the red box in

(j), and the blue dashed line indicates the phase boundary. (l-m) SAED pattern and atomic-resolution image of the α phase along the [010] zone axis acquired from the region outlined by the black dashed box in (k). (n-o) Fast Fourier transform (FFT) pattern and atomic-resolution image of the β phase along the [010] zone axis acquired from the region outlined by the green dashed box in (k).

3.3 Mechanical properties and fracture behavior

To evaluate the mechanical performance of SN-14, Fig. 6(a) presents the Vickers hardness as a function of applied load for SN-14 and the synthesized β- and γ-Si_3N_4 samples (experimental conditions are listed in Table 2). SN-14 exhibits a high Vickers hardness of 26.34 ± 0.61 GPa under a load of 19.6 N, demonstrating both excellent densification and effectiveness of the synthesis strategy. Nanoindentation measurements were subsequently performed under a load of 500 mN (Fig. S12 in the ESM). SN-14 exhibits a Young's modulus of 428.63 ± 7.89 GPa and a hardness of 34.40 ± 0.72 GPa, whereas γ-Si_3N_4 exhibits a Young's modulus of 572.84 ± 2.82 GPa and a hardness of 41.22 ± 1.04 GPa, consistent with previous reports [32]. The mechanical properties of β-Si_3N_4 were adopted from our previous work [31]. Based on these results, the fracture toughness values were calculated and compared with the Vickers hardness of α-, β-, and γ-Si_3N_4, as well as silicon nitride composite ceramics in Fig. 6(b) [23–26,30–32,56,59,60]. The corresponding testing conditions and relative densities are summarized in Table 3.

The introduction of γ phase, combined with the optimized sintering process, significantly improves the hardness of SN-14 compared with α- and β-Si_3N_4, while simultaneously retaining the toughening capability of β phase and maintaining a relatively high fracture toughness of 6.02 ± 0.48 $MPa \cdot m^{1/2}$. SEM observation further reveals a homogeneous microstructure, in which the gray γ phase and bright β phase (containing a small amount of α phase) are uniformly interwoven throughout the sample (Figs. 6(c)-6(e)). The fracture behavior is dominated by intergranular fracture, accompanied by continuous crack deflection, resulting in an overall zig-zag crack propagation path (Fig. 6(c)). Continuous crack arrest and reinitiation are observed at crack tips (Fig. 6(d)), indicating effective crack-shielding

capability. In regions of higher stress concentration, β grains with larger aspect ratios form robust crack bridges accompanied by crack branching, while pronounced crack arrest and reinitiation remain evident at the branch tips (Fig. 6(e)). These mechanisms collectively contribute to the enhanced fracture toughness of SN-14. Meanwhile, the γ phase serves as the primary high-hardness constituent, and its high hardness can be effectively exploited through the crystallographically well-bonded interfaces established by the sequential precipitation–densification mechanism. The resulting dense and well-bonded triphase microstructure enables the hard γ phase and toughening β phase to function synergistically, thereby achieving a favorable balance between hardness and fracture toughness.

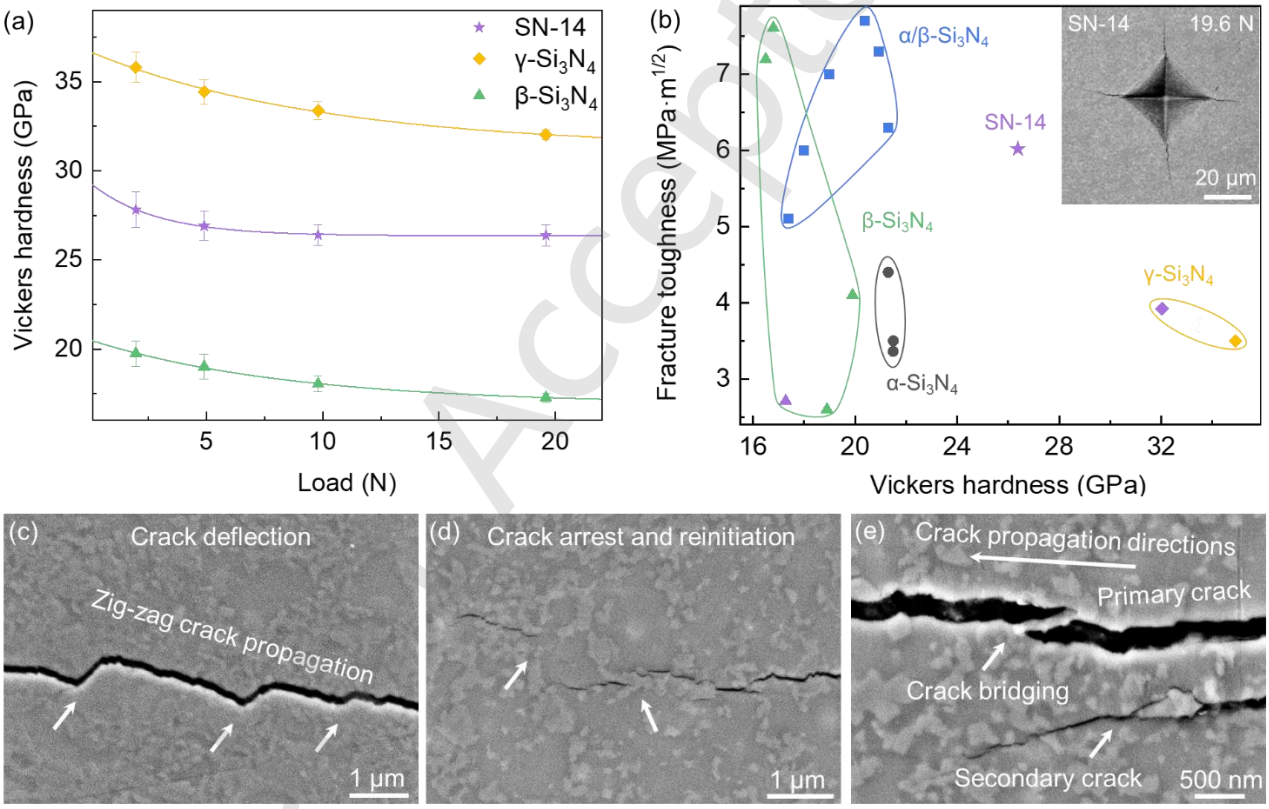

Fig. 6. Mechanical properties and fracture behavior of silicon nitride samples. (a) Vickers hardness of SN-14 and synthesized β- and γ-Si_3N_4 under different applied loads. (b) Comparison of Vickers hardness and fracture toughness among α-, β-, γ-Si_3N_4 and silicon nitride composite ceramics. All purple symbols represent samples synthesized in this work with the corresponding compositions. The inset (upper right) shows a representative indentation image of SN-14 under a load of 19.6 N. (c–e)

Representative crack propagation morphologies in SN-14, including crack deflection (c), crack arrest and reinitiation (d), and crack branching and bridging (e).

Table 3. Vickers hardness and fracture toughness of various silicon nitride ceramics. The values in parentheses following the Vickers hardness data indicate the corresponding indentation loads. For fracture toughness, "SENB" denotes the single-edge notched beam method, whereas numerical values indicate the indentation loads used for the Vickers indentation fracture (VIF) method.

Samples	Vicker hardness (GPa)	K_{IC} (MPa·m$^{1/2}$)	Relative density (%)	Reference
α-Si_3N_4	21.5±0.6 (4.9N)	3.5±0.2 (SENB)	98.7	23
	21.3±0.3 (49N)	4.4±0.2 (49N)	>99	24
	21.49±0.48 (98N)	3.36±0.62 (98N)	98.96	26
α/β-Si_3N_4	20.4±0.6 (4.9N)	7.7±0.6 (SENB)	98.3	23
	21.3±0.5 (49N)	6.3±0.3 (49N)	>99	24
	18 (98N)	6 (98N)	>98	30
	20.93±0.7 (49N)	7.3±0.35 (49N)	97.63	31
	19 (19.6N)	7 (19.6N)	>99	59
	17.4±0.4 (19.6N)	5.1±0.3 (19.6N)	98	60
β-Si_3N_4	16.5 (98N)	7.2 (98N)	96.7	25
	16.8±0.2 (98N)	7.61±0.42 (98N)	98.93	26
	19.9±0.7 (9.8N)	4.1±0.3 (9.8N)	97.1	56
	18.9±0.5 (9.8N)	2.6±0.3 (9.8N)	96.5	56
γ-Si_3N_4	34.9±0.7 (9.8N)	3.5±0.2 (9.8N)	~100	32
α/β/γ-Si_3N_4	26.34±0.61 (19.6N)	6.02±0.48 (19.6N)	98.4	This work
β-Si_3N_4	17.28±0.26 (19.6N)	2.71±0.24 (19.6N)	99.5	
γ-Si_3N_4	32.03±0.29 (19.6N)	3.92±0.21 (19.6N)	99.2	

4. Conclusions

In this work, the HPHT phase diagram of silicon nitride was systematically refined, revealing distinct α-to-γ and β-to-γ phase-transition pathways under high pressure. By exploiting the difference in their transition temperatures, a sequential precipitation–densification strategy was developed to construct a

homogeneous triphase in-situ composite ceramic (SN-14), with phase fractions of 21.3 wt.% α phase, 40.2 wt.% β phase, and 38.5 wt.% γ phase. SN-14 achieved a Vickers hardness of 26.34 ± 0.61 GPa and a fracture toughness of 6.02 ± 0.48 $MPa \cdot m^{1/2}$, demonstrating simultaneous enhancement of hardness and fracture toughness. More broadly, for ceramics with multiple polymorphs and accessible phase-transition pathways, controlling the transformation sequence and conditions may provide a general route to tailor phase composition, grain structures, and interfacial characteristics for targeted optimization of mechanical properties.

Acknowledgements

This work was supported by the Synergetic Extreme Condition User Facility (SECUF) Jilin Branch and Instrument and Equipment Sharing Platform, State Key Laboratory of High Pressure and Superhard Materials, Jilin University.

Funding

This work was supported by the National Natural Science Foundation of China (Nos. 12374201, U25A20192, and U2032215), the National Key R&D Program of China (No. 2023YFA1406200), Fundamental and Interdisciplinary Disciplines Breakthrough Plan of the Ministry of Education of China (JYB2025XDXM311), the Jilin Province Major Science and Technology Program, China (No. 20240211002GX), the Science and Technology Development Project of Jilin Province (No. SKL202402004), the Science and Technology Development Plan Project of Changchun, China (No. 23GZZ18), the Xiaomi Young Talents Program.

Author contributions

Shucheng Liu: Writing – original draft, Investigation, Methodology, Conceptualization, Validation, Visualization. **Bingtao Feng**: Visualization. **Zhaodong Liu**: Funding acquisition, Project

administration, Resources, Supervision. **Bingbing Liu**: Funding acquisition, Project administration, Resources, Supervision. **Hu Tang**: Writing – review and editing, Funding acquisition, Project administration, Resources, Supervision, Methodology, Conceptualization, Validation.

Availability of data and materials

The data that support the findings of this study are available from the corresponding author upon reasonable request.

Competing interests

The authors have no competing interests to declare that are relevant to the content of this article.

Electronic Supplementary Material

Supplementary material is available in the online version of this article**.**

References

[1] Padture NP. Advanced structural ceramics in aerospace propulsion. *Nat Mater* 2016, **15**: 804–9.

[2] Zinkle SJ, Busby JT. Structural materials for fission & fusion energy. *Mater Today* 2009, **12**: 12–9.

[3] Petzow G, Herrmann M. Silicon Nitride Ceramics. Jansen M, editor. In: High Performance Non-Oxide Ceramics II, Berlin, Heidelberg, Springer; 2002: 47–167.

[4] Krstic Z, Krstic VD. Silicon nitride: the engineering material of the future. *J Mater Sci* 2012, **47**: 535–52.

[5] Ji HM, Liang SM, Li YY, *et al.* An optimal match between platelet size and geometry in nacre to achieve its superior mechanical performance. *Trans Mater Res* 2026, **2**: 100165.

[6] Ritchie RO, Zheng XR. Growing designability in structural materials. *Nat Mater* 2022, **21**: 968–70.

[7] Eswarappa Prameela S, Pollock TM, Raabe D, *et al.* Materials for extreme environments. *Nat Rev Mater* 2023, **8**: 81–8.

[8] Dimas LS, Buehler MJ. Tough and stiff composites with simple building blocks. *J Mater Res* 2013, **28**: 1295–303.

[9] Bouville F, Maire E, Meille S, *et al.* Strong, tough and stiff bioinspired ceramics from brittle constituents. *Nat Mater* 2014, **13**: 508–14.

[10] Launey ME, Ritchie RO. On the fracture toughness of advanced materials. *Adv Mater* 2009, **21**: 2103–10.

[11] Clegg WJ, Kendall K, Alford NMcN, *et al.* A simple way to make tough ceramics. *Nature* 1990, **347**: 455–7.

[12] Cao X, Xu K, Yang J, *et al.* Fiber–Filler Size Matching Enables Toughening of Fine-Grained Isostatic Graphite. *Trans Mater Res* 2026, **2**: 100301.

[13] Garvie RC, Hannink RH, Pascoe RT. Ceramic steel? *Nature* 1975, **258**: 703–4.

[14] Lamon J, Mazerat S, R'Mili M. Reinforcement of Ceramic Matrix Composites: Properties of SiC-Based Filaments and Tows. In: Ceramic Matrix Composites, 2014: 1–26.

[15] Quinn JB, Quinn GD. Hardness and Brittleness of Ceramics. In: Proceedings of the 20th Annual Conference on Composites, Advanced Ceramics, Materials, and Structures—A: Ceramic Engineering and Science Proceedings, 1996: 59–68.

[16] Ritchie RO. The conflicts between strength and toughness. *Nat Mater* 2011, **10**: 817–22.

[17] Gavalda-Diaz O, Saiz E, Chevalier J, *et al.* Toughening of ceramics and ceramic composites through microstructure engineering: A review. *Int Mater Rev* 2025, **70**: 3–30.

[18] Faber KT, Evans AG. Crack deflection processes—I. Theory. *Acta Metall* 1983, **31**: 565–76.

[19] Cook J, Gordon JE. A mechanism for the control of crack propagation in all-brittle systems. *Proc R Soc Lond A* 1964, **282**: 508–20.

[20] Riley FL. Silicon Nitride and Related Materials. *J Am Ceram Soc* 2000, **83**: 245–65.

[21] Zerr A, Miehe G, Serghiou G, *et al.* Synthesis of cubic silicon nitride. *Nature* 1999, **400**: 340–2.

[22] Schwarz M, Miehe G, Zerr A, *et al.* Spinel-Si_3N_4: Multi-Anvil Press Synthesis and Structural Refinement. *Adv Mater* 2000, **12**: 883–7.

[23] Luo SC, Guo WM, Plucknett K, *et al.* Improved toughness of spark-plasma-sintered Si_3N_4 ceramics by adding HfB_2. *Ceram Int* 2021, **47**: 8717–21.

[24] Qin X, Zou J, Wang W, *et al.* High-pressure regulated phase transition enables in situ synthesis of high-performance dual-phase Si_3N_4 ceramics. *Sci China Mater* 2025, **68**: 4285–91.

[25] Yang X, Yang J, Xu X, *et al.* Injection molding of ultra-fine Si_3N_4 powder for gas-pressure sintering. *Int J Miner Metall Mater* 2015, **22**: 654–9.

[26] Tang SJ, Guo WM, Sun SK, *et al.* Design strategy of phase and microstructure of Si_3N_4 ceramics with simultaneously high hardness and toughness. *J Adv Ceram* 2023, **12**: 122–31.

[27] Kumar A, Gokhale A, Ghosh S, *et al.* Effect of nano-sized sintering additives on microstructure and mechanical properties of Si_3N_4 ceramics. *Mater Sci Eng A* 2019, **750**: 132–40.

[28] Liu N, Hu T, Fu Z, *et al.* Synergistic regulation of color and mechanical properties of silicon nitride ceramics via engineering hollow structures of Eu-enriched secondary phases. *Microstructures* 2024, **4**: 2024048.

[29] Yang H, Wang Z, Sun M, *et al.* Effect of pH, milling time, and Isobam content on porous silicon nitride ceramics prepared by gel casting. *Adv Powder Mater* 2023, **2**: 100060.

[30] Du S, Zhang J, Li F, *et al.* Effect of initial phase composition on the phase composition, microstructure, and mechanical properties of Si_3N_4 ceramics. *J Am Ceram Soc* 2024, **107**: 2556–64.

[31] Liu S, Pan Y, Feng B, *et al.* Toughening of silicon nitride ceramics through stress-induced phase transformation. *J Adv Ceram* 2025, **14**: 9221125.

[32] Nishiyama N, Ishikawa R, Ohfuji H, *et al.* Transparent polycrystalline cubic silicon nitride. *Sci Rep* 2017, **7**: 44755.

[33] Li W, Yu Z, Wiehl L, *et al.* Hard and tough novel high-pressure γ-Si_3N_4/Hf_3N_4 ceramic nanocomposites. *J Adv Ceram* 2023, **12**: 1418–29.

[34] Ge Y, Ma S, You C, *et al.* A distinctive HPHT platform with different types of large-volume press subsystems at SECUF. *Matter Radiat Extremes* 2024, **9**: 063801.

[35] Toby BH. EXPGUI, a graphical user interface for GSAS. *J Appl Crystallogr* 2001, **34**: 210–3.

[36] Yang H, Hu C, Zhou Y, *et al.* MatterSim: A Deep Learning Atomistic Model Across Elements, Temperatures and Pressures. *arXiv* 2024, arXiv:2405.04967.

[37] Song K, Zhao R, Liu J, *et al.* General-purpose machine-learned potential for 16 elemental metals and their alloys. *Nat Commun* 2024, **15**: 10208.

[38] Fan Z, Zeng Z, Zhang C, *et al.* Neuroevolution machine learning potentials: Combining high accuracy and low cost in atomistic simulations and application to heat transport. *Phys Rev B* 2021, **104**: 104309.

[39] Fan Z, Chen W, Vierimaa V, *et al.* Efficient molecular dynamics simulations with many-body potentials on graphics processing units. *Comput Phys Commun* 2017, **218**: 10–6.

[40] Xu K, Bu H, Pan S, *et al.* GPUMD 4.0: A high-performance molecular dynamics package for versatile materials simulations with machine-learned potentials. *Mater Genome Eng Adv* 2025, **3**: e70028.

[41] Sheppard D, Xiao P, Chemelewski W, *et al.* A generalized solid-state nudged elastic band method. *J Chem Phys* 2012, **136**: 074103.

[42] Hjorth Larsen A, Jørgen Mortensen J, Blomqvist J, *et al.* The atomic simulation environment—a Python library for working with atoms. *J Phys Condens Matter* 2017, **29**: 273002.

[43] Kresse G, Joubert D. From ultrasoft pseudopotentials to the projector augmented-wave method. *Phys Rev B* 1999, **59**: 1758–75.

[44] Blöchl PE. Projector augmented-wave method. *Phys Rev B* 1994, **50**: 17953–79.

[45] Perdew JP, Burke K, Ernzerhof M. Generalized Gradient Approximation Made Simple. *Phys Rev Lett* 1996, **77**: 3865–8.

[46] Grimme S, Antony J, Ehrlich S, *et al.* A consistent and accurate ab initio parametrization of density functional dispersion correction (DFT-D) for the 94 elements H-Pu. *J Chem Phys* 2010, **132**: 154104.

[47] Grimme S, Ehrlich S, Goerigk L. Effect of the damping function in dispersion corrected density functional theory. *J Comput Chem* 2011, **32**: 1456–65.

[48] Kresse G, Furthmüller J. Efficiency of ab-initio total energy calculations for metals and semiconductors using a plane-wave basis set. *Comput Mater Sci* 1996, **6**: 15–50.

[49] Kresse G, Furthmüller J. Efficient iterative schemes for ab initio total-energy calculations using a plane-wave basis set. *Phys Rev B* 1996, **54**: 11169–86.

[50] Anstis GR, Chantikul P, Lawn BR, *et al.* A Critical Evaluation of Indentation Techniques for Measuring Fracture Toughness: I, Direct Crack Measurements. *J Am Ceram Soc* 1981, **64**: 533–8.

[51] Kehren JT, Fischer M, Krause O. The Raman Spectra of α- and β-Si_3N_4 and Si_2N_2O Determined Experimentally and by Density Functional Theory. *J Raman Spectrosc* 2025, **56**: 155–64.

[52] Fang CM, de Wijs GA, Hintzen HT, *et al.* Phonon spectrum and thermal properties of cubic Si_3N_4 from first-principles calculations. *J Appl Phys* 2003, **93**: 5175–80.

[53] Soignard E, McMillan PF. Raman Spectroscopy of γ-Si_3N_4 and γ-Ge_3N_4 Nitride Spinel Phases Formed at High Pressure and High Temperature: Evidence for Defect Formation in Nitride Spinels. *Chem Mater* 2004, **16**: 3533–42.

[54] Xu B, Dong J, McMillan PF, *et al.* Equilibrium and metastable phase transitions in silicon nitride at high pressure: A first-principles and experimental study. *Phys Rev B* 2011, **84**: 014113.

[55] Jiang JZ, Kragh F, Frost DJ, *et al.* Hardness and thermal stability of cubic silicon nitride. *J Phys: Condens Matter* 2001, **13**: L515.

[56] Hou Z, Wang H, Yang Y, *et al.* High-pressure synthesis of high-performance submicron-sized polycrystalline β-Si_3N_4 bulk without additives. *Ceram Int* 2020, **46**: 12449–57.

[57] Nishiyama N, Langer J, Sakai T, *et al.* Phase relations in silicon and germanium nitrides up to 98 GPa and 2400 °C. *J Am Ceram Soc* 2019, **102**: 2195–202.

[58] Ma S, Zhao Y, Tang R, *et al.* Transparent β-Si_3N_4 and γ-Si_3N_4 compacts synthesized with mixed-size precursor under high pressure and high temperature. *Appl Phys Lett* 2021, **119**: 171904.

[59] Du S, Zhang J, Li F, *et al.* Rapid fabrication of Si_3N_4 ceramics with gradient appearance and microstructure. *J Am Ceram Soc* 2023, **106**: 7611–7.

[60] Andreev P, Drozhilkin P, Alekseeva L, *et al.* Spark Plasma Sintering of Si_3N_4 Ceramics with Y_2O_3–Al_2O_3 (3%–10% wt.) as Sintering Additive. *Coatings* 2023, **13**: 240.